Surface Functionalized Plasmonic Sensors for Uric Acid Detection With Gold-Graphene Stacked Nanocomposites

Olabisi Abdullahi ONIFADE[1,2], Dinie Dayana MOHAMAD AZRI[1], Muhammad Hafiz ABU BAKAR[1,2], Mohammed Thamer ALRESHEEDI[3], Eng Khoon NG[4], Mohd Adzir MAHDI[2,5], and Ahmad Shukri MUHAMMAD NOOR[1,2*]

[1]*Department of Computer and Communication Systems Engineering, Faculty of Engineering, Universiti Putra Malaysia, Serdang 43400, Malaysia*

[2]*Wireless and Photonics Research Centre of Excellence, Faculty of Engineering, Universiti Putra Malaysia, Serdang 43400, Malaysia*

[3]*Department of Electrical Engineering, College of Engineering, King Saud University, Riyadh 11421, Kingdom of Saudi Arabia*

[4]*Department of Engineering, University of Cambridge, Cambridge CB3 0FA, The United Kingdom*

[5]*Institute of Nanoscience and Nanotechnology (ION2), Universiti Putra Malaysia, Serdang 43400, Malaysia*

[*]Corresponding author: Ahmad Shukri MUHAMMAD NOOR E-mail: ashukri@upm.edu.my

Abstract: This study presented a surface-functionalized sensor probe using 3-aminopropyltriethoxysilane (APTES) self-assembled monolayers on a Kretschmann-configured plasmonic platform. The probe featured stacked nanocomposites of gold (via sputtering) and graphene quantum dots (GQD, via spin-coating) for highly sensitive and accurate uric acid (UA) detection within the physiological ranges. Characterization encompassed the field emission scanning electron microscopy for detailed imaging, energy-dispersive X-ray spectroscopy for elemental analysis, and Fourier transform infrared spectroscopy for molecular identification. Surface functionalization increased sensor sensitivity by 60.64%, achieving 0.022 1 °/(mg/dL) for the gold-GQD probe and 0.035 5 °/(mg/dL) for the gold-APTES-GQD probe, with linear correlation coefficients of 0.824 9 and 0.850 9, respectively. The highest sensitivity was 0.070 6 °/(mg/dL), with a linear correlation coefficient of 0.993 and a low limit of detection of 0.2 mg/dL. Furthermore, binding affinity increased dramatically, with the Langmuir constants of 14.29 μM^{-1} for the gold-GQD probe and 0.000 1 μM^{-1} for the gold-APTES-GQD probe, representing a 142 900-fold increase. The probe demonstrated notable reproducibility and repeatability with relative standard deviations of 0.166% and 0.013%, respectively, and exceptional temporal stability of 99.66%. These findings represented a transformative leap in plasmonic UA sensors, characterized by enhanced precision, reliability, sensitivity, and increased surface binding capacity, synergistically fostering unprecedented practicality.

Keywords: Plasmon; nanocomposite; gold-graphene quantum dot; uric acid, functionalize; sensor

Citation: Olabisi Abdullahi ONIFADE, Dinie Dayana MOHAMAD AZRI, Muhammad Hafiz ABU BAKAR, Mohammed Thamer ALRESHEEDI, Eng Khoon NG, Mohd Adzir MAHDI, *et al*., "Surface Functionalized Plasmonic Sensors for Uric Acid Detection With Gold-Graphene Stacked Nanocomposites," *Photonic Sensors*, 2025, 15(1), 250132.

Received: 27 March 2024 / Revised: 4 July 2024

DOI: 10.1007/s13320-024-0751-z
Article type: Regular

1. Introduction

Uric acid (UA), a common biomarker, is a waste product of purine breakdown [1, 2]. Physiologically typical UA levels are 2.0 mg/dL–7.5 mg/dL, applicable to both males and females [3]. Elevated UA levels can indicate gout, kidney disease, or certain cancers [4–6]. UA is also linked to chronic diseases such as cardiovascular disease, hypertension, and diabetes [7–9]. Monitoring UA levels aids in diagnosing medical conditions and identifying individuals at higher risk for chronic diseases.

Optical sensors detect changes using light, while biosensors employ biological molecules such as enzymes or antibodies to target specific analytes [10–12]. They consist of a recognition element and a transducer [13, 14], which converts the binding of specific biomolecules to measurable light-based signals, enabling the detection of proteins, nucleic acids, and small molecules [15, 16]. Optical biosensors play a crucial role in medical diagnostics, detecting disease biomarkers in patient samples to confirm diagnosis and monitor disease activity [17–21]. They can be categorized into surface plasmon resonance (SPR) biosensors [22], fiber optic biosensors [23–25], fluorescence biosensors [26–28], and the Raman biosensors [29–32].

SPR-based optical biosensors revolutionize biosensing, enabling highly sensitive and specific detection and quantification of biomolecules, by monitoring SPR signal shifts caused by changes in the refractive index at the metal-dielectric interface [33–35]. However, traditional SPR sensors, typically comprising single metal films, often lack the necessary sensitivity and selectivity for complex biological samples [36–38]. This limitation is particularly pronounced when attempting to detect low-concentration analytes such as UA. Certain SPR-based assays may yield false positives or false negatives, constraining their reliability for clinical applications.

In response to these challenges, our work presented a significant leap forward in the SPR biosensor technology. We have developed an innovative SPR sensor probe that integrated stacked nanocomposites made of gold and graphene quantum dots (GQD). This configuration not only boosted the sensor's sensitivity but also expanded its detection range to encompass both physiological and pathological UA levels found in human samples. The novelty of our approach lay in the strategic functionalization of the sensor probe's surface with self-assembled monolayers (SAM) of 3-aminopropyltriethoxysilane (APTES) [39, 40]. APTES served as a silane coupling agent that covalently binds to substrates, providing specific sites for nanoparticle attachment [41, 42]. This functionalization facilitated controlled nanoparticle orientation and distribution, resulting in a more stable and enhanced attachment compared to non-functionalized surfaces [43]. The sensor probe's performance was rigorously characterized using advanced techniques such as the field emission scanning electron microscopy (FESEM), energy dispersive X-ray spectroscopy (EDX), and Fourier transform infrared spectroscopy (FTIR). These methods confirmed the successful integration of nanocomposites onto the probe and validate its functionality. The remainder of this document is organized into three sections: Section 2 delves into the materials, protocols, and methodologies utilized in fabricating the sensor probe; Section 3 analyzes the results, focusing on performance metrics; Section 4 encapsulates the study's significant contributions and discusses its implications for enhancing clinical diagnostics.

2. Materials and methods

2.1 Reagents and resources

Glass coverslips (22 mm×22 mm×0.13 mm) from Sigma Aldrich (USA) were used to fabricate the sensing probe. To remove organic contaminants and residues from the sensing surface, the piranha

solution was prepared using hydrogen peroxide (H_2O_2) and sulfuric acid (H_2SO_4) from Sigma Aldrich. APTES and ethanol from Sigma Aldrich were used to functionalize the glass coverslips. Gold targets and GQD (ACS Material, USA) were used to immobilize the nanocomposites on the glass coverslips. UA powder and sodium chloride (NaCl) from Sigma Aldrich were used to prepare the analyte solution for measuring the performance of the sensor probe. Acetone and ethanol were used throughout for processing, storing, and cleaning the glass coverslips before use in each step. Deionized (DI) water was used throughout the experiment. Concentration adjustments were made using the relation $C_1V_1=C_2V_2$ to achieve the desired concentrations. All materials were handled with clean gloves and tweezers to prevent contamination. Most of the reagents were of analytical grade and purchased from Sigma-Aldrich.

2.2 Surface functionalization with APTES

Glass coverslips were functionalized with the SAM of APTES to introduce amino groups and increase active sites for UA interaction with the gold-GQD stacked nanocomposites [44, 45]. As shown in Fig. 1, the glass coverslips were immersed in the piranha solution (1:3 v/v mixture of H_2SO_2 and H_2SO_4) for 30 minutes, rinsed with DI water, and dried in a vacuum oven at 70 ℃ for 1 hour to remove organic residues and introduce hydrophilicity. A 1% APTES solution was prepared by mixing 1 mL of APTES and 99 mL of the ethanol solvent. The coverslips were immersed in the APTES solution for 24 hours, sonicated in ethanol to remove any unreacted APTES, rinsed with DI water, and dried in the oven at 90 ℃ for 2 hours. The functionalized sensor probes were stored in a sealed container before the gold film deposition with a desiccant at room temperature to maintain a dry environment and prevent any hydrolysis and degradation of the functional groups.

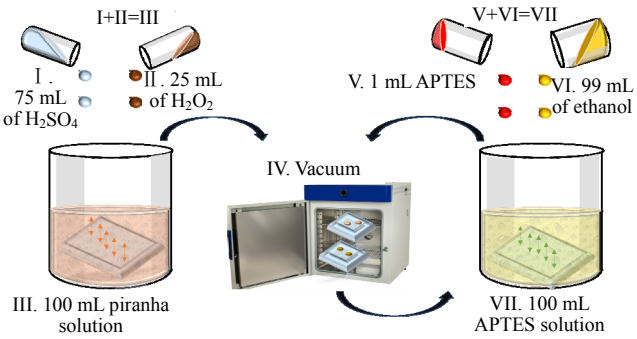

Fig. 1 Surface functionalization of the sensor probe.

2.3 Immobilization of gold-GQD nanocomposite

The functionalized sensor probe underwent gold film deposition through the sputtering technique to fortify the facilitation of surface plasmons. This method was chosen for its ability to create pristine, impurity-free films, ensuring the final product's performance [46, 47]. Additionally, it produced thin films with exceptional uniformity, providing precise control over the thickness and composition compared to other deposition methods like thermal evaporation, electroplating, and chemical vapor deposition [48].

Gold films with the thickness in the range of 50 nm were successfully deposited using a sputter coater (EMITECH K575X, Quorum Technologies, UK) with a deposition rate of 0.746 nm/s as shown in Fig. 2. The sputter time was set to 67 seconds, while the sputter current was maintained at 30 mA, the voltage was kept at 2.2 kV, and the clean current was set to 130 mA. The outcomes align seamlessly with prior findings detailed in [49, 50], affirming the targeted thickness, morphology, and purity as corroborated in Section 3.2 of this current study.

Subsequently, the carboxyl groups of GQD, intended for binding to the amino groups of UA were introduced to the sensor probe's surface via a spin coater (TB616, China), leading to the creation of a stacked nanocomposite, as illustrated in Fig. 2. The GQD was synthesized through the hydrothermal method, emitting 460 nm blue light under 365 nm UV excitation, with purity exceeding 70% and a

particle size below 10 nm [51]. Spin coating was chosen for its speed, simplicity, uniformity, and controlled film thickness compared to methods like dip coating or spray coating [52, 53].

The glass side of the sensor probe was affixed to the spin coater chuck, and by utilizing a micropipette, 0.5 mL of the GQD solution was precisely applied to the central region of the sensing surface. Following a 30-minute incubation period to enhance binding affinity, the coverslips were spun at 2 000 rpm for 70 seconds. Subsequent removal of residual GQD solution drops was followed by oven-drying the coverslips at 90 ℃ for 45 minutes. The sensor probe underwent a final step of annealing on a hot plate at 300 ℃ for 15 minutes, enhancing intermolecular bonding within the stacked nanocomposite and stabilizing the carboxyl groups on the sensor probe's surface.

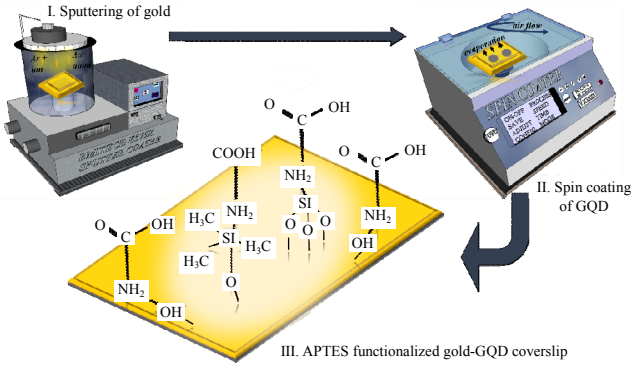

Fig. 2 Immobilization of the stacked nanocomposites on the sensor probe.

2.4 Preparation of UA solution

The UA solution concentrations of 0.5 mg/dL, 1 mg/dL, 5 mg/dL, 8 mg/dL, and 12 mg/dL were prepared by diluting UA powder in DI water. The UA powder was precisely weighed on a digital balance and transferred to a sanitized, desiccated beaker. DI water and sodium chloride were added gradually to aid UA powder dissolution, and additional DI water was added to reach the desired concentration. The solution was stirred at 300 rpm using a magnetic stirrer for 30 minutes to ensure uniform dispersion. The prepared UA solution was hermetically sealed and stored at 4 ℃ until use.

2.5 Characterization and evaluation

The functional groups and chemical bonds within the stacked nanocomposites were elucidated using the Fourier transform infrared spectroscopy (FTIR) in the ATR mode (Bruker, USA). Additionally, imaging of the sensor probe, including surface morphology and material composition, was accomplished with FESEM (NOVA, NANOSEM 230, USA) and EDX (X-MAX, Oxford Instruments, UK).

The efficacy of the SPR sensor probe for UA solution detection was assessed using the experimental setup depicted in Fig. 3. The configuration consisted of a sensor probe, a sample injection mechanism, an optical apparatus, a stepper motor (NEWPORT MM 3000, USA), and a lock-in amplifier (SR 530, SRS, USA). The instruments were carefully calibrated to ensure precise resonance angle detection and reflection intensity monitoring. Varied UA solution concentrations were sequentially introduced into the flow cell containing the sensor probe, triggering the formation of complexes on its surface. The optical system, comprising laser light (He-Ne, 632.8 nm), a prism (SF 11, USA), a photodetector, a chopper (SR 540, SRS, USA), a filter, and a pinhole, efficiently generated surface plasmon waves on the coated sensor probe's surface. The prism coupled the light, enabling the photodetector to measure reflected light intensity—a key metric for bound UA molecules. The chopper modulated light intensity for enhanced signal clarity, while a filter minimized background noise interference, ensuring data integrity. Changes in the refractive index and corresponding light reflection alterations were dynamically tracked by the photodetector and analyzed using MATLAB and Microsoft Excel on the desktop computer (OPTIPLEX 755, USA).

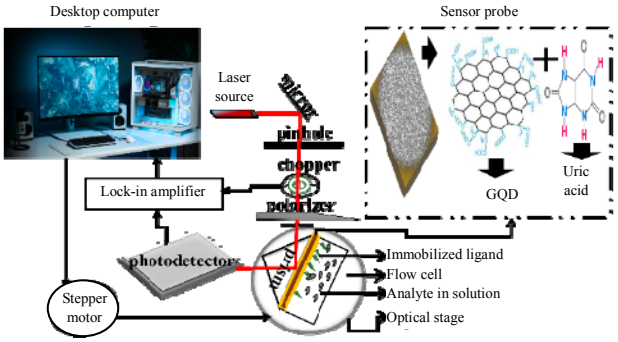

Fig. 3 SPR sensor experiment setup.

3. Results and discussion

3.1 FTIR characterization

The structural features of the gold-GQD and gold-APTES-GQD nanocomposites were probed using FTIR spectroscopy. In the wavenumber range of 4 000 cm^{-1} to 600 cm^{-1}, the anticipated functional groups were observed, thus validating the structures of all samples, as illustrated in Fig. 4. The FTIR spectrum of the gold-GQD nanocomposite in Fig. 4(a) revealed peaks occurring around 3 311.56 cm^{-1}, 2 141.41 cm^{-1}, and 1 636.57 cm^{-1} which was attributed to the characteristic O–H stretching vibration [54]. The spectral bands at wavenumbers of 3 075 cm^{-1}, 2 867 cm^{-1}, 2 145 cm^{-1}, 1 767 cm^{-1}, and 1 150 cm^{-1}–1 616 cm^{-1} were attributed to the following vibrational modes: C–H stretching (alkene), C–H stretching (alkane), indicative of the presence of polycyclic aromatic hydrocarbons, C–N stretching, C=O stretching, and C–O stretching, respectively [55, 56].

Concurrently, observing the FTIR spectrum of gold-APTES-GQD nanocomposite in Fig. 4(b), a prominent absorption peak, localized at approximately 1 099.75 cm^{-1}, was identified and attributed to the existence of Si–O–C and Si–O–Si chemical bonds. This spectral feature was indicative of the extended Si–O–Si network, originating from the structural configuration of the APTES molecules [57]. The absorption peak at 1 436.01 cm^{-1} was attributed to the presence of C–N bonds, stemming from amines or amides [58]. The peak occurring at 1 636.57 cm^{-1} was indicative of functional groups such as NH_2, NH, or C=C. At 1 734.87 cm^{-1}, the absorption peak was conclusively assigned to C=O bonds, signifying the existence of amide or carboxyl functional groups [59]. The observed spectral features encompassing the wavenumbers between 2 943.77 cm^{-1} and 2 870 cm^{-1} were reasonably ascribed to C–H stretching modes, stemming from the C–O–C configuration, while the spectral region from 3 400 cm^{-1} to 3 300 cm^{-1} could be predominantly attributed to the O–H stretching vibrations of water molecules or the symmetric/asymmetric NH stretching modes inherent to the APTES compound [60]. These results confirmed the successful functionalization of the sensor probe.

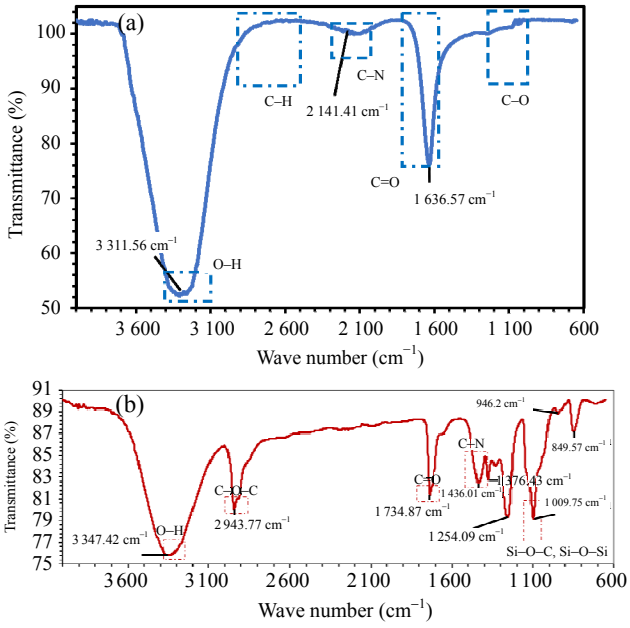

Fig. 4 FTIR spectrum for (a) gold-GQD nanocomposite and (b) gold-APTES-GQD nanocomposite.

3.2 FESEM and EDX characterization

Transverse-sectional FESEM images for the stacked nanocomposites along with EDX images showing their elemental compositions are illustrated in Figs. 5(a) and 5(b). The FESEM visuals revealed an average thickness of about 60 nm for the stacked nanocomposites of the sensor probe, thereby validating the efficacy of the sputtering deposition

methods employed for the gold film in Section 2.3. The EDX graphical portrayals in Fig. 5(b) exhibit prominent peaks corresponding to silicon (Si), carbon (C), and gold (Au) material elements, affirming their predominant presence and even distribution in both sensor probe configurations.

FESEM micrographs depicting surface morphology at 25 000× magnifications with dimensions of 1 μm–4 μm are presented in Fig. 6. The discrepancy in luminance detected in both configurations could be ascribed to the presence of GQD in the stacked nanocomposite, given that elements possessing higher atomic numbers yielded more intensified signals [61]. The microporous structure observed in Fig. 6(a) for the functionalized sensor probe was more complex than that of the non-functionalized sensor probe observed in Fig. 6(b) owing to the silane molecules linking to neighboring molecules. These images provided a comprehensive depiction of the sensor probe structures, affirming the homogeneous distribution of gold-GQD nanocomposites across the sensor probe's surface.

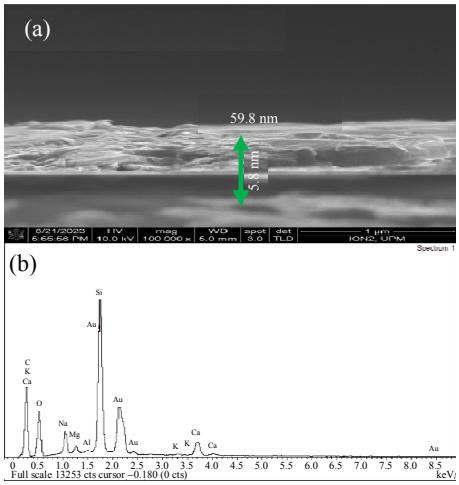

Fig. 5 Stacked nanocomposite's (a) transverse sectional FSEEM image and (b) EDX image.

3.3 Binding kinetics

The binding interaction between the UA solution and GQD on the sensor probe's surface was assessed using a non-linear fitting technique based on the

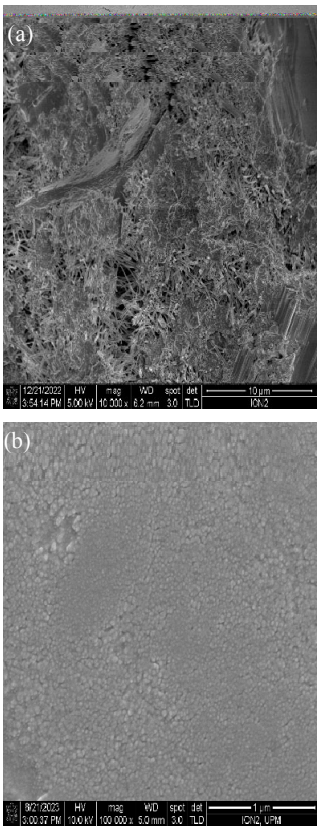

Fig. 6 Surface morphology: (a) functionalized sensor probe and (b) non-functionalized sensor probe.

Langmuir adsorption isotherm model expressed with (1) [62, 63]:

$$\Delta\theta_{\mathrm{RES}} = \frac{\Delta\theta_{\mathrm{RES}_{\max}} C}{K_D + C} \tag{1}$$

where θ_{RES} is the angle shift of the SPR curve at equilibrium, $\Delta\theta_{\mathrm{RES}_{\max}}$ is the maximum angle shift at saturation, C is the concentration of the UA solution, and K_D is the Langmuir dissociation constant. From Fig. 7, the Langmuir constants for the gold-GQD probe and gold-APTES-GQD probe were 14.29 μM^{-1} and 0.000 1 μM^{-1}, respectively, yielding binding affinities of ($7\times10^4\ M^{-1}$) and $10^{10}\ M^{-1}$ accordingly. These results indicated that the sensor probe's functionalization with the SAM of APTES significantly enhanced the binding affinity for the UA solution adsorption, with an enhancement factor of about 142 900. The maximum adsorption capacity of the gold-APTES-GQD probe was also substantially higher than that of the gold-GQD probe.

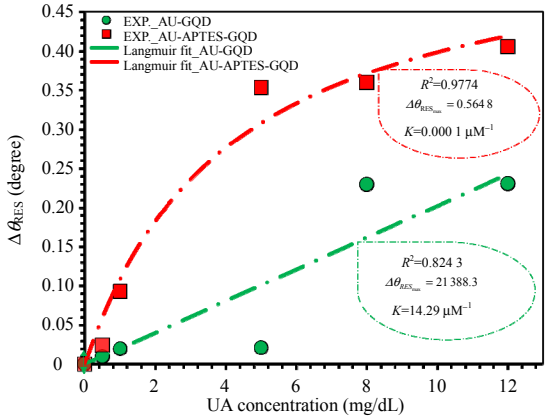

Fig. 7 Langmuir isotherm model for the gold-GQD and gold-APTES-GQD sensor probes.

Owing to the limitation of homogeneity in binding sites associated with the Langmuir model, further analysis of the binding kinetics was carried out using the Sips isotherm model written with (2) [64, 65]:

$$\Delta\theta_{RES} = \frac{\Delta\theta_{RES_{max}} KC^n}{1 + KC^n} \quad (2)$$

where K is the sips isotherm model affinity constant, C is the UA solution concentration, and n is the heterogeneity constant. The illustrations in Fig. 8 shows that the presence of the SAM of APTES in the gold-APTES-GQD probe increases its heterogeneity constant and correlation coefficients. These results were in good agreement with those obtained using the Langmuir model.

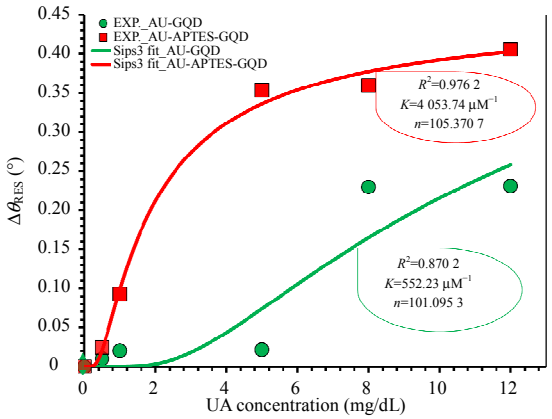

Fig. 8 Sips adsorption isotherm model for the gold-GQD and gold-APTES-GQD sensor probes.

3.4 UA detection and quantitation

Figures 9, 10, and 11 present SPR reflectivity plots obtained using the gold-GQD probe and the gold-APTES-GQD probe to measure the baseline signal and UA solution concentrations ranging from 0 mg/dL to 12 mg/dL. The initial step involved injecting 1 mL of DI water into the flow cell, to establish the baseline resonant angle. It was determined by scanning the SPR signal curve dips in Fig. 9 and marking the angular position. Following this, 1 mL of each UA solution concentration was sequentially introduced into the flow cell. The resonant angle shift for each concentration was monitored for both the gold-GQD probe and gold-APTES-GQD probe. It involved scanning the SPR signal curve dips and recording their angular positions in Figs. 10 and 11, respectively. All resonant angle measurement for DI water and different UA solution concentrations was recorded in Table 1 for further analysis and comparison between the two sensor probes.

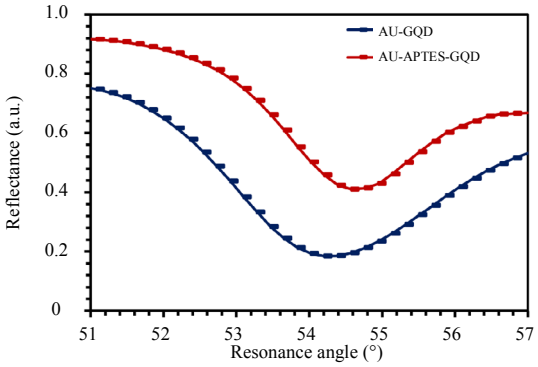

Fig. 9 SPR reflectivity plots for gold-GQD and gold-APTES-GQD sensor probes measuring DI water.

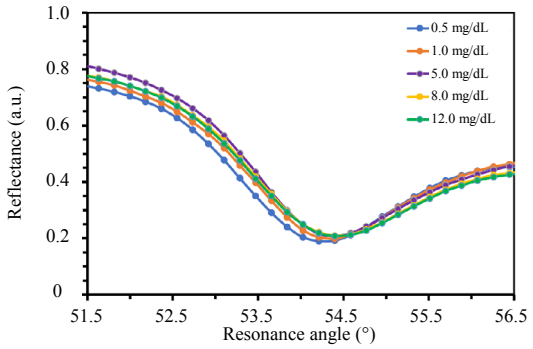

Fig. 10 SPR reflectivity plots for the gold-GQD sensor probe measuring different UA solution concentrations.

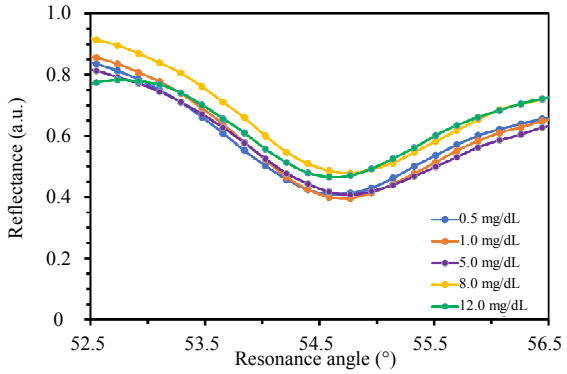

Fig. 11 SPR reflectivity plots for the gold-APTES-GQD sensor probe measuring different UA solution concentrations.

Table 1 Resonant angles of the sensor probes for different UA solution concentrations.

Sensor probe	UA concentration (mg/dL)	Resonance angle (°)
Gold-GQD	DI	54.210 0
	0.5	54.220 0
	1.0	54.230 0
	5.0	54.423 1
	8.0	54.440 0
	12.0	54.441 1
Gold-APTES-GQD	DI	54.579 9
	0.5	54.606 7
	1.0	54.672 7
	5.0	54.933 4
	8.0	54.939 8
	12.0	54.985 8

The sensitivity (S), which is the sensor probe's ability to detect small changes in the refractive index on its surface was calculated using (3), representing the ratio of the change in SPR angle ($\Delta\theta_{RES}$) to the change in the UA solution concentration [66]:

$$S = \frac{\Delta\theta_{RES}}{UA_{concentration}}. \quad (3)$$

To evaluate the sensitivity of each probe, linearity plots were generated for UA solution concentrations ranging from 0 mg/dL to 12 mg/dL. These plots are shown in Fig. 12(a) for the gold-GQD probe and Fig. 12(b) for the gold-APTES-GQD probe. The results demonstrated that $\Delta\theta_{RES}$ increases with increasing the UA solution concentration for both sensor configurations. Notably, the gold-GQD probe exhibited a sensitivity of 0.022 1°/(mg/dL), while the gold-APTES-GQD probe boasted a higher 0.035 5°/(mg/dL). This superior performance of the gold-APTES-GQD probe was further corroborated by its higher linear correlation coefficient of 0.850 9 compared to the gold-GQD probe's 0.824 9. The data points in Figs. 12(a) and 12(b) were fitted to mathematical models represented with (4) and (5), respectively.

$$\Delta\theta_{RES} = -0.273\,4\Delta p \times \exp\left(-\frac{c}{3.356\,6}\right) + 0.251\,8 \quad (4a)$$

$$R^2 = 0.970\,6 \quad (4b)$$

$$\Delta\theta_{RES} = -0.431\,1\Delta p \times \exp\left(-\frac{c}{3.060\,3}\right) + 0.411\,5 \quad (5a)$$

$$R^2 = 0.998\,7 \quad (5b)$$

where Δp is the magnitude of the resonance angle change and c is the UA solution concentration.

The bolstered sensitivity for the gold-APTES-GQD probe was most pronounced at lower UA solution concentrations ranging from 0.5 mg/dL to 5 mg/dL, reaching the sensitivity of 0.070 6°/(mg/dL) with an impressive linear correlation coefficient of 0.992 8 as shown in Fig. 13. Its enhanced performance at these lower bounds could be attributed to a reduction in readily available binding sites at higher UA concentrations, leading to a saturation effect.

The limit of detection (LOD), representing the minimum variation in the UA solution concentration reliably detectable by the functionalized sensor probe, was calculated with (6) [67]:

$$LOD = \frac{3SD_{blank\_solution}}{S}. \quad (6)$$

The standard deviation (SD) of the blank solution was determined by measuring DI water ten times each with the developed gold-APTES-GQD probe. This resulted in an SD of 0.002 4 and a calculated LOD of 0.2 mg/dL.

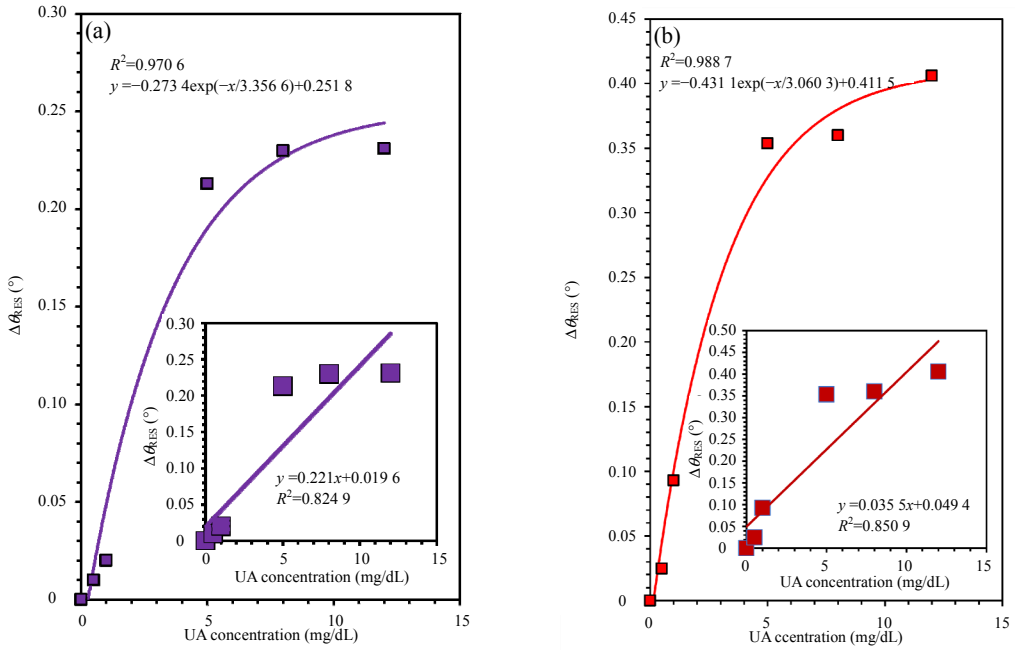

Fig. 12 Fitting curves and linearity plots for the (a) gold-GQD sensor probe and (b) gold-APTES-GQD sensor probe.

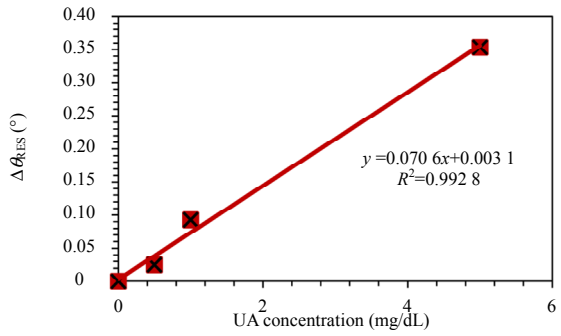

Fig. 13 Linearity plots of the gold-APTES-GQD sensor probe for 1 mg/dL–5 mg/dL of UA solution concentration.

The performance of the developed gold-APTES-GQD sensor probe was comprehensively compared with prior studies on UA sensing using the SPR technique in terms of sensitivity, binding affinity, detection range, and LOD. The results obtained are summarized in Table 2. It demonstrated superior sensitivity, binding affinity, and LOD in contrast to earlier investigations, registering values of 0.035 5°/(mg/dL), 1.6×10^{8} $(mg/dL)^{-1}$, and 0.2 mg/dL, respectively. The heightened sensitivity, binding affinity, and LOD observed in the developed sensor probe for detecting UA, especially within the physiologically relevant concentration ranges, could be attributed to the distinctive properties of the SAM of APTES. It increased the surface functionality and availability of active binding sites for UA solution adsorption on the sensor surface. Additionally, the angular interrogation mode, unique to this study employed a simpler and more cost-effective setup compared to the more commonly used wavelength interrogation technique [68]. While previous research employing the angular interrogation mode has shown a promising minimum enhancement factor of 3.6 for both surface and bulk refractive index sensitivity compared to dual-mode SPR sensors utilizing wavelength interrogation [69], further investigation is necessary to conclusively confirm its superiority in sensitivity, specifically for UA solution detection. This will necessitate using identical sensor configurations for comparing both techniques in a controlled environment specifically tailored to UA sensing.

Table 2 Comparison of sensing performance of SPR-based sensors for UA detection.

Sensor configuration	Interrogation mode	Sensitivity	Binding affinity $(mg/dL)^{-1}$	Detection range (mg/dL)	LOD (mg/dL)	Ref.
Optical fiber/Ag/Si	Wavelength	0.625 nm/(mg/dL)	—	0–15.13	0.053 8	[70]
Kretschmann: hybrid AU-ZnO	FDTD simulation	0.001 7 °/(mg/dL)	—	0–50	10.1	[71]
Tapered fiber/AUNP/GO	Wavelength	0.482 nm/(mg/dL)	—	0.17–13.45	3.46	[72]
Kretschmann: UA imprinted Poly(HEMA-MAC)-Fe^{3+}NPs/Au/prism	Intensity	0.001 8 %/(mg/dL)	0.007 2	0.05–4	0.025	[73]
Tapered plastic optical fiber/ZnO	Intensity	0.025 mV/(mg/dL)	—	0–50	0.56	[74]
Micro-ball fiber/AUNP/GO	Intensity	0.125 %/(mg/dL)	—	0.168–15.13	1.103	[75]
Tapered fiber/AUNP/uricase	Wavelength	0.435 nm/(mg/dL)	—	0.168–15.13	2.96	[76]
Kretschmann: AU-GQD/prism	Intensity	3.77 %/(mg/dL)	0.667	1–9	4.74	[49]
Kretschmann: AU–APTES–GQD/prism	Angular	0.035°5 °/(mg/dL)	1.6×10^{8}	0.5–12	0.2	This work

3.5 DA, SNR, and FOM

The FWHM of the developed sensor probe, which represents the width of the SPR signal curve at half of its peak intensity, was used to assess the probe's precision. The detection accuracy (DA) is inversely related to FWHM and can be expressed with (7) [77, 78]:

$$\mathrm{DA} = \frac{1}{\mathrm{FWHM}}. \tag{7}$$

As shown in Fig. 14(a), FWHM increased with increasing the UA solution concentration up to 8 mg/dL due to the heightened sensor surface bulk thickness. This hindered precise resonant angle detection, causing laser light attenuation and broadening of the SPR curve [79, 80]. Beyond 8 mg/dL, this effect diminished.

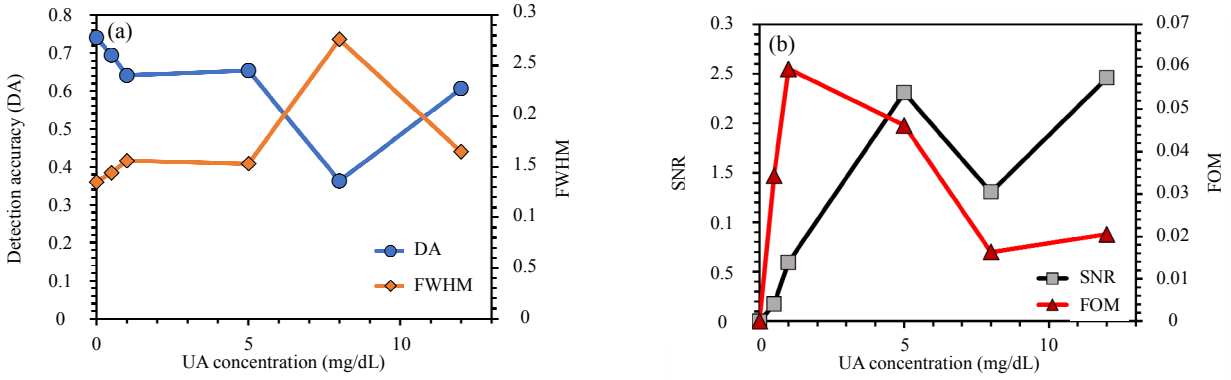

Fig. 14 Functionalized sensor's probe: (a) DA and FWHM for different UA solution concentrations and (b) SNR and FOM for different UA solution concentrations.

The SNR of the sensor probe was used to gauge its signal strength against the background noise. To ensure reliable measurement, a minimum SNR of 3:1 was indispensable, calculable using (8) [81]:

$$\mathrm{SNR} = \frac{\Delta\theta_{\mathrm{RES}}}{\mathrm{FWHM}}. \tag{8}$$

Elevating UA concentrations correlated with reduced noise in the SPR signal curves, manifesting as higher SNR values in the sensor probe as

illustrated in Fig. 14(b). This phenomenon arose from changes in the sensor film's refractive index due to increased UA concentrations, facilitating enhanced UA binding on the sensor surface. This observation aligned with the findings in [82, 83], albeit with a distinct analyte.

Reliable detection hinged on maintaining a high FOM for the sensor, which combined sensitivity, specificity, and dynamic range. FOM can be calculated using (9) [84]:

$$\mathrm{FOM} = \frac{S}{\mathrm{FWHM}}. \tag{9}$$

From Fig. 14(b), FOM and SNR values initially increased with the UA solution concentration up to 1 mg/dL, before decreasing at 5 mg/dL and 8 mg/dL, and increasing again at 12 mg/dL. The higher FOM at this concentration might be due to reduced metal dissipation after surface plasmon activation at a shorter wavelength, constraining the FWHM. The subsequent decline could be attributed to a faster loss in sensor sensitivity compared to changes in DA as the UA solution concentration increased.

3.6 Reproducibility, repeatability, and stability tests

The developed sensor probe's reproducibility, reflecting consistent result generation, was assessed across eight batches of probes produced with refined parameters. Testing each probe with a 12 mg/dL UA solution yielded a remarkably low relative standard deviation (RSD) of 0.166% as shown in Fig. 15(a), indicative of high methodological consistency.

For reusability, a probe with optimized parameters measured a 12 mg/dL UA solution ten times, showing a minimal RSD of 0.013% as shown in Fig. 15(b). This underscored the substantial reusability of the probe and its procedures, contributing to cost reduction and waste minimization.

Durability assessment over a month, exposed to a 12 mg/dL UA solution, revealed an initial steady resonance angle of 54.589 8 for five days. A slight deviation to 54.96° occurred after one week and was maintained until the third week. A decline to 54.579 9 in the third week aligned with baseline signal measurement. This value persisted until the fourth week, indicating the sensor probe retained 99.95% effectiveness for the first week and sustained 99.66% efficiency for three weeks as shown in Fig. 15(c). However, by the end of one month, the probe lost its sensing capability.

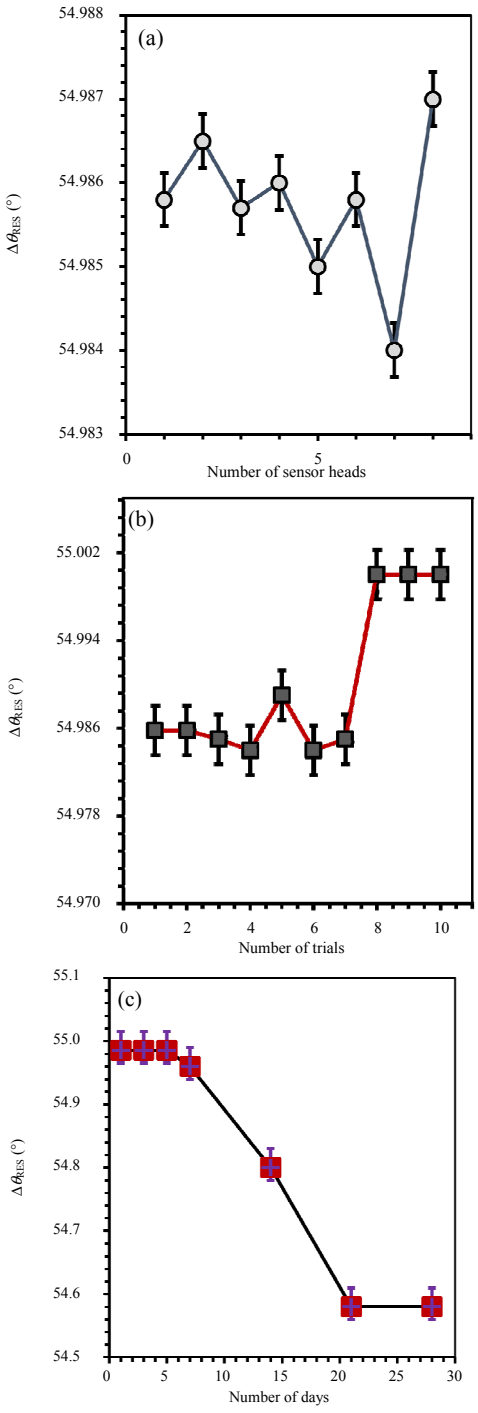

Fig. 15 Functionalized sensor's probe: (a) reproducibility, (b) repeatability, and (c) stability tests.

4. Conclusions

This study developed a sensor probe with gold-GQD stacked nanocomposites, functionalized with the SAM of APTES, for precise measurement of UA solution concentrations typically found in human body fluids. Surface analysis using FESEM and EDX validated the nanocomposite thickness and composition. FTIR analysis characterized the structural features and functional groups, revealing key bonds like O–H, C=O, C–H, C–N, and C–O, and NH stretching modes of APTES. Adsorption isotherm data analyzed with the Langmuir and sips isotherm model showed a 142 900-fold increase in binding affinity, with the Langmuir constants of 14.29 μM^{-1} for gold-GQD and 0.000 1 μM^{-1} for gold-APTES-GQD probes. Sensitivity increased by 60.64%, reaching values of 0.022 1 °/(mg/dL) and 0.035 5 °/(mg/dL) for gold-GQD and gold-APTES-GQD probes, respectively, with corresponding linearities of 0.824 9 and 0.850 9. At lower UA concentrations, the peak sensitivity of 0.070 6 °/(mg/dL) was achieved with a linearity of 0.992 8. The DA increased linearly with the UA concentration, and FWHM decreased correspondingly, indicating improved precision and resolution. An anomaly at 8 mg/dL had no impact on sensor performance. SNR and FOM improved linearly at lower UA concentrations, but decreased sensitivity at higher concentrations. The probe demonstrated excellent reproducibility and repeatability, with RSD values of 0.166% and 0.013%, respectively, maintaining 99.66% of its sensing capacity over three weeks. The introduction of APTES SAM enhanced surface functionality, resulting in increased binding sites, sensitivity, binding affinity, and reduced LOD. Consequently, it markedly improved the sensor's overall performance, enabling precise detection of abnormal UA concentrations, particularly at low levels, thereby addressing a broad spectrum of health conditions effectively.

Acknowledgment

This work was supported by the Ministry of Higher Education Malaysia under the Fundamental Research Grant Scheme (Grant No. FRGS/1/2019/TK05/UPM/02/5) and the King Saud University, Kingdom of Saudi Arabia, under the Researchers Supporting Project (Grant No. RSP2024R336).

Declarations

Conflict of Interest The authors declare that they have no competing interests.

Permissions All the included figures, tables, or text passages that have already been published elsewhere have obtained the permission from the copyright owner(s) for both the print and online format.

References

[1] M. Jin, F. Yang, I. Yang, Y. Yin, J. J. Luo, H. Wang, *et al*., "Hyperuricemia and vascular diseases," *Front Biosci*, 2012, 17(2): 656–669.

[2] R. El Ridi and H. Tallima, "Physiological functions and pathogenic potential of uric acid: a review," *Journal of Advances Research*, 2017, 8(5): 487–493.

[3] W. Yu and J. D. Cheng, "Uric acid and cardiovascular disease: an update from molecular mechanism to clinical perspective," *Front Pharmacol*, 2020, 16(11): 582680.

[4] B. N. Ames, R. Cathcart, E. Schwiers, and P. Hochstein, "Uric acid provides an antioxidant defense in humans against oxidant- and radical-caused aging and cancer: a hypothesis," *Proceedings of the National Academy of Sciences of the United States of America*, 1981, 78(11): 6858–6862.

[5] J. Maiuolo, F. Oppedisano, S. Gratteri, C. Muscoli, and V. Mollace, "Regulation of uric acid metabolism and excretion," *International Journal of Cardiology*, 2016, 213: 8–14.

[6] F. Braga, S. Pasqualetti, S. Ferraro, and M. Panteghini, "Hyperuricemia as risk factor for

coronary heart disease incidence and mortality in the general population: a systematic review and meta-analysis," *Clinical Chemistry and Laboratory Medicine*, 2016, 54(1): 7–15.

[7] M. Boban, G. Kocic, S. Radenkovic, R. Pavlovic, T. Cvetkovic, M. Deljanin-Ilic, *et al*., "Circulating purine compounds, uric acid, and xanthine oxidase/dehydrogenase relationship in essential hypertension and end stage renal disease," *Renal Failure*, 2014, 36(4): 613–618.

[8] J. P. Forman, H. Choi, and G. C. Curhan, "Uric acid and insulin sensitivity and risk of hypertension," *Archives Internal Medicine*, 2009, 169(2): 155–162.

[9] P. Bjornstad, L. Laffel, J. Lynch, L. El Ghormli, R. S. Weinstock, S. E. Tollefsen, *et al*., "Elevated serum uric acid is associated with greater risk for hypertension and diabetic kidney diseases in obese adolescents with type 2 diabetes: an observational analysis from the treatment options for type 2 diabetes in adolescents and youth (today) study," *Diabetes Care*, 2019, 42(6): 1120–1128.

[10] P. S. Adarakatti, K. Sureshkumar, and T. Ramakrishnappa, "Carbon nanomaterial-based sensors: an efficient tool in the environmental sectors," *Carbon Nanomaterials-Based Sensors: Emerging Research Trends in Devices and Applications*, 2022: 149–165.

[11] R. İlktaç and E. Henden, "Molecularly imprinted polymer-based optical sensors for pesticide determination," *Molecular Imprinting for Nanosensors and Other Sensing Applications*, 2021: 93–115.

[12] L. Eddaif and A. Shaban, "*Fundamentals of sensor technology*," in Advanced Sensor Technology: Biomedical, Environmental, and Construction Applications, A. Barhoum and Z. Altintas, Eds., Elsevier, 2023: 17–49.

[13] P. Damborský, J. Švitel, and J. Katrlík, "Optical biosensors," *Essays Biochem*, 2016, 60(1): 91–100.

[14] D. Dey and T. Goswami, "Optical biosensors: a revolution towards quantum nanoscale electronics device fabrication," *Journal of Biomedicine and Biotechnology*, 2011, 2011: 348218.

[15] C. S. Law, L. F. Marsal, and A. Santos, "*Electrochemically engineered nanoporous photonic crystal structures for optical sensing and biosensing*," in Handbook of Nanomaterials in Analytical Chemistry: Modern Trends in Analysis, C. M. Hussain, Eds., Elsevier, 2019: 201–226.

[16] M. Nejadmansouri, M. Majdinasab, G. S. Nunes, and J. L. Marty, "An overview of optical and electrochemical sensors and biosensors for analysis of antioxidants in food during the last 5 years," *Sensors*, 2021, 21(4): 1176.

[17] S. Akgönüllü and A. Denizli, "*Recent advances in optical biosensing approaches for biomarkers detection*," Biosens Bioelectron X12 (2022) 100269, Available at https://doi.org/10.1016/J.BIOSX.2022.100269.

[18] J. Tai, S. Fan, S. Ding, and L. Ren, "Gold nanoparticles based optical biosensors for cancer biomarker proteins: a review of the current practices," *Frontiers in Bioengineering and Biotechnology*, 2022, 10: 877193.

[19] M. H. Son, S. W. Park, H. Y. Sagong, and Y. K. Jung, "Recent advances in electrochemical and optical biosensors for cancer biomarker detection," *BioChip Journal*, 2023, 17: 44–67.

[20] A. J. Haes, L. Chang, W. L. Klein, and R. P. Van Duyne, "Detection of a biomarker for Alzheimer's disease from synthetic and clinical samples using a nanoscale optical biosensor," *Journal of the American Chemical Society*, 2005, 127(7): 2264–2271.

[21] A. Gharatape and A. Y. Khosroushahi, "Optical biomarker-based biosensors for cancer/infectious disease medical diagnoses," *Applied Immunohistochemistry and Molecular Morphology*, 2019, 27(4): 278–286.

[22] J. H. Park, Y. W. Cho, and T. H. Kim, "Recent advances in surface plasmon resonance sensors for sensitive optical detection of pathogens," *Biosensors*, 2022, 12(3): 180.

[23] L. Zeni, C. Perri, N. Cennamo, F. Arcadio, G. D'Agostino, M. Salmona, *et al*., "A portable optical-fibre-based surface plasmon resonance biosensor for the detection of therapeutic antibodies in human serum," *Scientific Reports*, 2020, 10: 11154.

[24] S. E. Mowbray and A. M. Amiri, "A brief overview of medical fiber optic biosensors and techniques in the modification for enhanced sensing ability," *Diagnostics*, 2019, 9(1): 23.

[25] L. Singh, N. Agarwal, H. Barthwal, B. Arya, and T. Singh, "*Application of fiber optics in bio-sensing*," in Fiber Optics-Technology and Applications, G. Huerta-Cuellar, Eds., London: IntechOpen, 2021.

[26] A. Camarca, A. Varriale, A. Capo, A. Pennacchio, A. Calabrese, C. Giannattasio, *et al*., "Emergent biosensing technologies based on fluorescence spectroscopy and surface plasmon resonance," *Sensors*, 2021, 21(3): 906.

[27] H. Qu, C. Fan, M. Chen, X. Zhang, Q. Yan, Y. Wang, *et al*., "Recent advances of fluorescent biosensors based on cyclic signal amplification technology in biomedical detection," *Journal of Nanobiotechnology*, 2021, 19: 403.

[28] D. Koveal, C. M. Díaz-García, and G. Yellen, "Fluorescent biosensors for neuronal metabolism and the challenges of quantitation," *Current Opinion Neurobiology*, 2020, 63: 111–121.

[29] S. Yang and J. D. Zahn, "*Biosensors using surface-enhanced Raman scattering*," in Encyclopedia of Microfluidics and Nanofluidics, D.

Q. Li, Eds., Boston: Springer, 2008: 120–127.
[30] I. Notingher, "Raman spectroscopy cell-based biosensors," *Sensors*, 2007, 7(8): 1343–1358.
[31] K. V. Serebrennikova, A. N. Berlina, D. V. Sotnikov, B. B. Dzantiev, and A. V. Zherdev, "Raman scattering-based biosensing: new prospects and opportunities," *Biosensors*, 2021, 11(12): 512.
[32] P. Chauhan, A. Bhargava, R. Kumari, P. Ratre, R. Tiwari, R. K. Srivastava, *et al*., "Surface-enhanced Raman scattering biosensors for detection of oncomiRs in breast cancer," *Drug Discovery Today*, 2022, 27(8): 2121–2136.
[33] J. Pollet, F. Delport, K. P. F. Janssen, K. Jans, G. Maes, H. Pfeiffer, *et al*., "Fiber optic SPR biosensing of DNA hybridization and DNA-protein interactions," *Biosensors and Bioelectronics*, 2009, 25(4): 864–869.
[34] Y. Iwasaki, T. Horiuchi, and O. Niwa, "Detection of electrochemical enzymatic reactions by surface plasmon resonance measurement," *Analytical Chemistry*, 2001, 73(7): 1595–1598.
[35] H. H. Nguyen, J. Park, S. Kang, and M. Kim, "Surface plasmon resonance: a versatile technique for biosensor applications," *Sensors*, 2015, 15(5): 10481–10510.
[36] J. B. Maurya, Y. K. Prajapati, V. Singh, J. P. Saini, and R. Tripathi, "Improved performance of the surface plasmon resonance biosensor based on graphene or MoS_2 using silicon," *Optics Communications*, 2016, 359: 426–434.
[37] S. Aksimsek, H. Jussila, and Z. Sun, "Graphene-MoS_2-metal hybrid structures for plasmonic biosensors," *Optics Communications*, 2018, 428: 233–239.
[38] M. S. Rahman, M. R. Hasan, K. A. Rikta, and M. S. Anower, "A novel graphene coated surface plasmon resonance biosensor with tungsten disulfide (WS_2) for sensing DNA hybridization," *Optical Materials*, 2018, 75: 567–573.
[39] E. Wijaya, C. Lenaerts, S. Maricot, J. Hastanin, S. Habraken, J. P. Vilcot, *et al*., "Surface plasmon resonance-based biosensors: from the development of different SPR structures to novel surface functionalization strategies," *Current Opinion in Solid State and Materials Science*, 2011, 15(5): 208–224.
[40] J. A. Howarter and J. P. Youngblood, "Optimization of silica silanization by 3-aminopropyltriethoxysilane," *Langmuir*, 2006, 22(26): 11142–11147.
[41] E. T. Vandenberg, L. Bertilsson, B. Liedberg, K. Uvdal, R. Erlandsson, H. Elwing, *et al*., "Structure of 3-aminopropyl triethoxy silane on silicon oxide," *Journal of Colloid and Interface Science*, 1991, 147(1): 103–118.
[42] W. Wang and M. W. Vaughn, "Morphology and amine accessibility of (3-aminopropyl) triethoxysilane films on glass surfaces," *Scanning*, 2008, 30(2): 65–77.
[43] M. Ghorbanpour and C. Falamaki, "A novel method for the fabrication of ATPES silanized SPR sensor chips: exclusion of Cr or Ti intermediate layers and optimization of optical/adherence properties," *Applied Surface Science*, 2014, 301: 544–550.
[44] X. Wu, S. Guo, and J. Zhang, "Selective oxidation of veratryl alcohol with composites of Au nanoparticles and graphene quantum dots as catalysts," *Chemical Communications*, 2015, 51(29): 6318–6321.
[45] Y. Yang, J. Zhang, F. Zhang, and S. Guo, "Preparation of AuNPs/GQDs/SiO_2 composite and its catalytic performance in oxidation of veratryl alcohol," *Journal of Nanomaterials*, 2017, 2017(1): 4130569.
[46] A. H. Simon, "*Sputter processing*," in Handbook of Thin Film Deposition (Fourth Edition), K. Seshan and D. Schepis, Eds., New York: William Andrew Publishing, 2018: 195–230.
[47] D. Depla, S. Mahieu, and J. E. Greene, "*Sputter deposition processes*," in Handbook of Deposition Technologies for Films and Coatings (Third Edition): Science, Applications and Technology, P. M. Martin, Eds., New York: William Andrew Publishing, 2009: 253–296.
[48] N. Y. Abu-Thabit and A. S. H. Makhlouf, "*Fundamental of smart coatings and thin films: synthesis, deposition methods, and industrial applications, advances in smart coatings and thin films for future industrial and biomedical engineering application*," Amsterdam: Elsevier, 2020: 3–35.
[49] O. A. Onifade, Z. H. M. Zin, M. H. B. A. Bakar, M. T. Alresheedi, M. A. Bin Mahdi, and A. S. M. Noor, "Salivary uric acid detection with graphene-gold bilayers surface plasmon resonance," *IEEE Sensors Journal*, 2023, 23(22): 27186–27198.
[50] O. A. Onifade, F. A. Yusairie, M. H. A. Bakar, M. T. Alresheedi, E. K. Ng, M. A. Mahdi, *et al*., "Uricase biofunctionalized plasmonic sensor for uric acid detection with APTES-modified gold nanotopping," *Biosensors and Bioelectronics*, 2024, 261(1): 116486.
[51] N. I. M. Fauzi, Y. W. Fen, F. B. K. Eddin, W. M. E. M. M. Daniyal, "Structural and optical properties of graphene quantum dots-polyvinyl alcohol composite thin film and its potential in plasmonic sensing of carbaryl," *Nanomaterials*, 2022, 12(22): 4105.
[52] U. G. Lee, W. B. Kim, D. H. Han, H. S. Chung, "A modified equation for thickness of the film fabricated by spin coating," *Symmetry*, 2019, 11(9): 1183.
[53] D. Pan, J. Zhang, Z. Li, and M. Wu, "Hydrothermal route for cutting graphene sheets into blue-luminescent graphene quantum dots," *Advanced Materials*, 2010, 22(6): 734–738.

[54] A. Bokare, D. Nordlund, C. Melendrez, R. Robinson, O. Keles, A. Wolcott, *et al*., "Surface functionality and formation mechanisms of carbon and graphene quantum dots," *Diamond and Related Materials*, 2020, 110: 108101.

[55] S. Yang, C. Zhu, J. Sun, P. He, N. Yuan, J. Ding, *et al*., "Triphenylphosphine modified graphene quantum dots: spectral modulation for full spectrum of visible light with high quantum yield," *RSC Advances*, 2015, 5(42): 33347–33350.

[56] G. M. Paternò, Goudappagouda, Q. Chen, G. Lanzani, F. Scotognella, and A. Narita, "Large polycyclic aromatic hydrocarbons as graphene quantum dots: from synthesis to spectroscopy and photonics," *Advanced Optical Materials*, 2021, 9(23): 2100508.

[57] J. Kim, P. Seidler, L. S. Wan, and C. Fill, "Formation, structure, and reactivity of amino-terminated organic films on silicon substrates," *Journal of Colloid and Interface Science*, 2009, 329(1): 114–119.

[58] K. H. Kale and S. S. Palaskar, "Plasma enhanced chemical vapor deposition of tetraethylorthosilicate and hexamethyldisiloxane on polyester fabrics under pulsed and continuous wave discharge," *Journal of Applied Polymer Science*, 2012, 125(5): 3996–4006.

[59] C. Volcke, R. P. Gandhiraman, V. Gubala, J. Raj, T. Cummins, G. Fonder, *et al*., "Reactive amine surfaces for biosensor applications, prepared by plasma-enhanced chemical vapour modification of polyolefin materials," *Biosensors and Bioelectronics*, 2010, 25(8): 1875–1880.

[60] X. Rao, A. A. Hassan, C. Guyon, M. Zhang, S. Ognier, and M. Tatoulian, "Plasma polymer layers with primary amino groups for immobilization of nano- and microparticles," *Plasma Chemistry and Plasma Processing*, 2020, 40: 589–606.

[61] B. Lewczuk and N. Szyryńska, "Field-emission scanning electron microscope as a tool for large-area and large-volume ultrastructural studies," *Animals*, 2021, 11(12): 3390.

[62] W. Ye, Y. Q. Pan, L. J. He, B. Q. Chen, J. J. Liu, J. Gao, *et al*., "*Design with modeling techniques*," in Industrial Ventilation Design Guidebook (Volume 2): Engineering Design and Applications (Second Edition), H. D. Goodfellow and Y. Wang, Eds., San Diego: Academic Press, 2021: 109–183.

[63] K. A. VanDer Kamp, D. Qiang, A. Aburub, and D. E. Wurster, "Modified langmuir-like model for modeling the adsorption from aqueous solutions by activated carbons," *Langmuir*, 2005, 21(1): 217–224.

[64] K. Y. Foo and B. H. Hameed, "Insights into the modeling of adsorption isotherm systems," *Chemical Engineering Journal*, 2010, 156(1): 2–10.

[65] S. Azizian and S. Eris, "Adsorption isotherms and kinetics," *Interface Science and Technology*, 2021, 33: 445–509.

[66] N. A. Jamil, G. S. Mei, N. B. Khairulazdan, S. P. Thiagarajah, A. A. Hamzah, B. Y. Majlis, *et al*., "Detection of uric acid using kretschmann-based SPR biosensor with MoS_2-graphene," in *2018 IEEE 16th Student Conference on Research and Development*, Selangor, 2018, pp. 1–4.

[67] L. Rana, R. Gupta, M. Tomar, and V. Gupta, "Highly sensitive Love wave acoustic biosensor for uric acid," *Sensors and Actuators B: Chemical*, 2018, 261: 169–177.

[68] H. Koresawa, K. Seki, K. Nishimoto, E. Hase, Y. Tokizane, T. A. Yano, *et al*., "Real-time hybrid angular-interrogation surface plasmon resonance sensor in the near-infrared region for wide dynamic range refractive index sensing," *Scientific Reports*, 2023, 13: 15655.

[69] J. Guo, J. T. Hastings, and P. D. Keathley, "Dual-mode surface-plasmon-resonance sensors using angular interrogation," *Optics Letters*, 2008, 33(5): 512–514.

[70] R. Kant, R. Tabassum, and B. D. Gupta, "Fiber optic SPR-based uric acid biosensor using uricase entrapped polyacrylamide gel," *IEEE Photonics Technology Letters*, 2016, 28(9): 2050–2053.

[71] S. N. Mustaffa, N. Md Yatim, A. R. Abdul Rashid, N. Md Yatim, V. Pithaih, N. S. Sha'ari, *et al*., "Visible and angular interrogation of Kretschmann-based SPR using hybrid Au-ZnO optical sensor for hyperuricemia detection," *Heliyon*, 2023, 9(12): e22926.

[72] L. Singh, R. Singh, B. Zhang, S. Cheng, B. Kumar Kaushik, and S. Kumar, "LSPR based uric acid sensor using graphene oxide and gold nanoparticles functionalized tapered fiber," *Optical Fiber Technology*, 2019, 53: 102043.

[73] A. Sarıkaya, B. Osman, T. Çam, and A. Denizli, "Molecularly imprinted surface plasmon resonance (SPR) sensor for uric acid determination," *Sensors and Actuators B: Chemical*, 2017, 251: 763–772.

[74] M. Batumalay, Z. Harith, H. A. Rafaie, F. Ahmad, M. Khasanah, S. W. Harun, *et al*., "Tapered plastic optical fiber coated with ZnO nanostructures for the measurement of uric acid concentrations and changes in relative humidity," *Sensors and Actuators A: Physical*, 2014, 210: 190–196.

[75] S. Kumar, R. Singh, G. Zhu, Q. Yang, X. Zhang, S. Cheng, *et al*., "Development of uric acid biosensor using gold nanoparticles and graphene oxide functionalized micro-ball fiber sensor probe," *IEEE Transactions on NanoBioscience*, 2020, 19(2): 173–182.

[76] L. Singh, G. Zhu, R. Singh, B. Zhang, W. Wang, B. K. Kaushik, *et al*., "Gold nanoparticles and uricase functionalized tapered fiber sensor for uric acid detection," *IEEE Sensors Journal*, 2020, 20(1): 219–226.

[77] M. Salari and H. R. Askari, "Theoretical investigation of absorption and sensitivity of nano-plasmonic fiber optic sensors," *Optics & Laser*

Technology, 2013, 48: 315–325.

[78] F. Mumtaz, M. Roman, B. Zhang, L. G. Abbas, M. A. Ashraf, M. A. Fiaz, *et al*., "A simple optical fiber SPR sensor with ultra-high sensitivity for dual-parameter measurement," *IEEE Photonics Journal*, 2022, 14(5): 6852907.

[79] N. A. S. Omar, R. Irmawati, Y. W. Fen, E. N. Muhamad, F. B. K. Eddin, N. A. A. Anas, *et al*., "Surface refractive index sensor based on titanium dioxide composite thin film for detection of cadmium ions," *Measurement*, 2022, 187: 110287.

[80] A. S. Kushwaha, A. Kumar, R. Kumar, and S. K. Srivastava, "A study of surface plasmon resonance (SPR) based biosensor with improved sensitivity," *Photonics and Nanostructures–Fundamentals and Applications*, 2018, 31: 99–106.

[81] T. B. A. Akib, S. F. Mou, M. M. Rahman, M. M. Rana, M. R. Islam, I. M. Mehedi, *et al*., "Design and numerical analysis of a graphene-coated SPR biosensor for rapid detection of the novel coronavirus," *Sensors*, 2021, 21(10): 3491.

[82] F. B. Kamal Eddin, Y. W. Fen, J. Y. C. Liew, N. I. M. Fauzi, W. M. E. M. M. Daniyal, and H. Abdullah, "Development of plasmonic-based sensor for highly sensitive and selective detection of dopamine," *Optics & Laser Technology*, 2023, 161: 109221.

[83] N. A. S. Omar, Y. W. Fen, J. Abdullah, A. R. Sadrolhosseini, Y. M. Kamil, N. I. M. Fauzi, *et al*., "Quantitative and selective surface plasmon resonance response based on a reduced graphene oxide-polyamidoamine nanocomposite for detection of dengue virus E-proteins," *Nanomaterials*, 2020, 10(3): 569.

[84] Q. Q. Meng, X. Zhao, C. Y. Lin, S. J. Chen, Y. C. Ding, and Z. Y. Chen, "Figure of merit enhancement of a surface plasmon resonance sensor using a low-refractive-index porous silica film," *Sensors*, 2017, 17(8): 1846.